

Importance of Terrain Representation in Simulating a Stationary Convective System for the July 2017 Northern Kyushu Heavy Rainfall Case

Tetsuya Takemi

Disaster Prevention Research Institute, Kyoto University, Uji, Japan

Abstract

An extreme, damaging rainfall occurred in northern Kyushu in July 2017. Whether such an extreme rainfall is quantitatively captured by numerical models is a challenging issue. We investigate the influences of terrain representation in simulating a stationary convective system and the resulting heavy rainfall for this case by conducting a series of 167-m-resolution numerical experiments. By employing a high-resolution elevation dataset as well as a double-moment cloud microphysics scheme, the control experiment successfully reproduced the stationary, linear-shaped convective system and the associated heavy rainfall. When the model terrain was created by a coarser-resolution elevation dataset, the 167-m-resolution experiment underestimated the accumulated rainfall, because of discretely developing convection and weaker intensities of the rainfall. These impacts of the terrain representation were confirmed to be robust through conducting another experiments with a different microphysics scheme. The representation of model terrains is critically important in simulating stationary convective systems and quantitatively the resulting heavy rainfall.

(Citation: Takemi, T., 2018: Importance of terrain representation in simulating a stationary convective system for the July 2017 Northern Kyushu Heavy Rainfall case. *SOLA*, 14, 153–158, doi:10.2151/sola.2018-027.)

1. Introduction

Stationary convective systems are one of the major extreme-rain-producing storms. Schumacher and Johnson (2005) examined extreme rain events in the United States and found that a back-building/quasi-stationary type accounts for about 20% of the total mesoscale convective system (MCS) events largely contributing to extreme rainfalls. Schumacher and Johnson (2008) indicated that the long-lived nature of the MCS was due to a nearly stationary low-level gravity wave, suggesting that both mesoscale and convective-scale processes play a role in keeping MCSs stationary.

Furthermore, topography is known to have profound effects on precipitation (Houze 2010). In East Asia a stationary front during the summer monsoon is a major player in spawning extreme rainfalls, possibly enhanced by topography. For example, a complex nature of the topography of Taiwan significantly controls the generation and organization of MCSs (Wang et al. 2005; Yu and Jou 2005; Yu and Lin 2008; Wang et al. 2014). Yoshizaki et al. (2000) examined an orographic rainband in western Kyushu, Japan and showed that small and low mountains are able to generate an organized rainband under a moist convectively unstable condition. A role of small-scale topography on the generation of orographic rainbands was also emphasized by Kirshbaum et al. (2007), who indicated that small-scale obstacles induce lee waves and trigger convection downstream of the obstacles.

From a statistical point of view, Tsuguti and Kato (2014) examined warm-season heavy rain events in Japan and suggested that there is a topographical influence on the generation of stationary rain events. Unuma and Takemi (2016a) examined stationary

meso- β -scale convective systems, called as quasi-stationary convective clusters (QSCCs), during the warm season and mentioned that the locations of QSCC occurrence correspond to regions with high elevation.

From these studies, the topography, even if it is in small scales, seems to contribute to the generation of stationary convective systems and hence to the resulting heavy rainfalls. A scientific challenge exists how numerical models can reproduce stationary convective systems and quantitatively represent the resulting heavy rainfalls. For wind representations, Oku et al. (2010), Takemi et al. (2010), and Takemi (2013) demonstrated that accurate representations of fine topographical features improve the representations of extreme winds in complex terrain. For rainfall, Takemi (2010) and Oizumi et al. (2018) showed that the simulation with finer terrains reproduced stronger rains. However, there are few studies that examined how topographical representations affect quantitative simulations of heavy rainfalls.

This study investigates the influences of fine terrain features on the generation of stationary convective systems and the resulting heavy rainfalls by conducting a $O(100\text{ m})$ -resolution simulation with a high-resolution elevation dataset as well as a number of sensitivity experiments changing the model terrain and the model physics. A heavy rainfall case that occurred in northern Kyushu, Japan in July 2017 (the July 2017 Northern Kyushu Heavy Rainfall) was chosen. This case produced extreme rainfalls in northern Kyushu and spawned damaging floods and landslides. The primary challenge here is whether the simulation represents the stationarity of the extreme-rain-producing convective system and quantitatively reproduces the extreme rainfall.

2. Numerical model and experimental design

The model used is the Weather Research and Forecasting (WRF) model Version 3.6.1 (Skamarock et al. 2008). Two-way nesting was used to set four computational domains: the outermost domain (Domain 1) covers most of the Japanese islands at the 4.5-km horizontal grid, the second domain (Domain 2) Kyushu Island at the 1.5-km grid, the third domain (Domain 3) the northern half of Kyushu Island at the 500-m grid, and the innermost domain (Domain 4) focuses northern Kyushu at the 167-m grid (see Fig. A1 of Supplement 1). Domain 1 was defined in the Lambert conformal projection on the plane crossing the latitudes of 30°N and 60°N. The four domains had 52 vertical levels, with the interval stretched with height and the top at the 30-hPa level. To prescribe the initial and boundary conditions, we used the Mesoscale Analysis of Japan Meteorological Agency for the atmospheric fields and the Final Analysis of National Centers for Environmental Prediction for the surface fields, both at 6-hour interval.

The model topography was generated with a coarser-resolution digital elevation model (DEM) dataset and a higher-resolution DEM dataset. The topography in Domain 1 and 2 was generated with the global DEM data having a horizontal grid spacing of 30 arc-seconds (about 1 km) (referred to as G30) provided by the United States Geological Survey, while the topography in Domain 3 and 4 was created with the 50-m horizontal resolution DEM data provided by the Geospatial Information Authority of Japan (referred to as GSI); this GSI dataset is a digital version of the GSI maps created by ground-based measurements. The generated

Corresponding author: Tetsuya Takemi, Disaster Prevention Research Institute, Kyoto University, Gokasho, Uji, Kyoto 611-0011, Japan. E-mail: takemi@storm.dpri.kyoto-u.ac.jp.

©The Author(s) 2018. This is an open access article published by the Meteorological Society of Japan under a Creative Commons Attribution 4.0 International (CC BY 4.0) license (<http://creativecommons.org/licenses/by/4.0>).



topography is shown in Fig. A1 of Supplement 1. To examine the sensitivity to the choice of the elevation dataset, we used the G30 data to create the model topography not only in Domain 1 and 2 but also in Domain 3 and 4 and conducted sensitivity experiments (see Fig. A2 in Supplement 1).

The physics parameterizations used as a baseline were as follows: the Yonsei University scheme for boundary-layer mixing (Hong et al. 2006), a Monin-Obukhov similarity-based scheme for surface fluxes (Jimenez et al. 2012), and a double-moment scheme for cloud microphysics (Morrison et al. 2009). No cumulus parameterization was used. The experiment with these physics settings and the GSI elevation is regarded as the control and referred to as MODM-GSI, while the experiment with the same physics settings but with the G30 terrain is referred to as MODM-G30.

To demonstrate the robustness of the terrain representation in reproducing the heavy rainfall, we conducted further sensitivity experiments with the microphysics scheme changed to the 6-category single-moment scheme of Hong and Lim (2006); other physics parameterizations were unchanged from the control. This series of the sensitivity experiments are referred to as WSM6-GSI for the GSI terrain and WSM6-G30 for the G30 terrain.

All in all, four numerical experiments were conducted. The time integration was started at 0900 Japan Standard Time (JST) 4 July 2017 for Domain 1 and 2, 2100 JST 4 July for Domain 3, and 0300 JST 5 July and ended at 0900 JST 7 July. The time interval

of the simulated outputs for Domain 4 is 10 minutes. These outputs are used for the following analyses.

3. Reproduction of the stationary convective system

The case developed under influences of a stationary front (i.e., Baiu front, see Fig. A3 of Supplement 1 for the weather maps): during the southward movement of the Baiu front the heavy rainfall occurred. Among the raingauge stations, the heaviest rainfall was measured at the Asakura station: the maximum accumulated rainfalls for 24, 48, and 72 hours were 545.5 mm (by 1140 JST 6 July), 600.5 mm (by 1040 JST 7 July), and 616.0 mm (by 0600 JST 7 July), respectively, all of which are the highest records at the station. Figure 1a shows the total rainfall from 0300 JST 5 July to 0900 JST 7 July from radar/raingauge analyzed precipitation data (Nagata 2011). Some points indicate extreme values exceeding 1000 mm, and a robust feature is that the area with rainfall over 500 mm extends west-east. This is consistent with the climatology shown by Unuma and Takemi (2016b): the orientation of linear convective systems align favorably in the west-east direction in northern Kyushu. In this section, the result of the control, MODM-GSI, is demonstrated.

Figure 1b exhibits the accumulated rainfall simulated in Domain 4 during the same period as in Fig. 1a. The area with over 500 mm rainfall also extends longitudinally, and the pointwise maximum rainfall amounts to 633 mm. Although the simulation overall underestimated the observed rainfall, it successfully reproduced the spatial pattern and concentrated nature of the extreme rainfall.

Figure 2 compares the temporal change of the simulated rainfall in Domain 4 with the observed at Asakura. The observed accumulated rainfall largely increases during 1200 and 2100 JST 5 July and then gradually increases until 0900 JST 7 July (Fig. 2a). The simulated rainfall at the Asakura gridpoint indicates an increase from 1200 to 2100 JST 5 July, but this increase is more gradual than the observed. This is because the simulation is not able to reproduce the exact location of rainfalls. However, if the time series at the gridpoint of the maximum rainfall, about 16.6

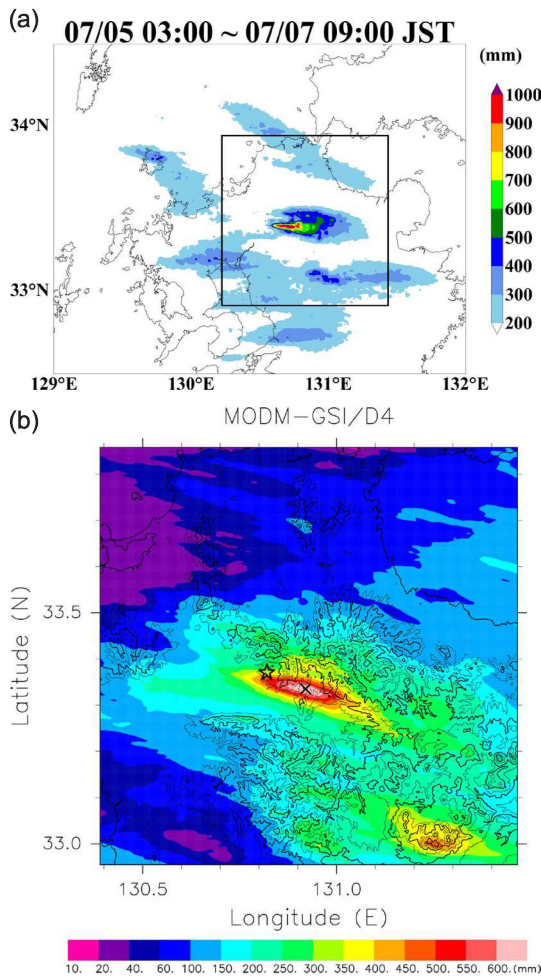


Fig. 1. The accumulated rainfall from 0300 JST 5 July to 0900 JST 7 July 2017 from (a) the gridded precipitation analysis and (b) the control experiment MODM-GSI in Domain 4. The box in (a) indicates the region shown in (b). In (b), the contour lines indicate the surface elevation at the 200-m interval, and the star and the cross marks denote the locations of the Asakura grid point and the point of the maximum accumulated rainfall, respectively.

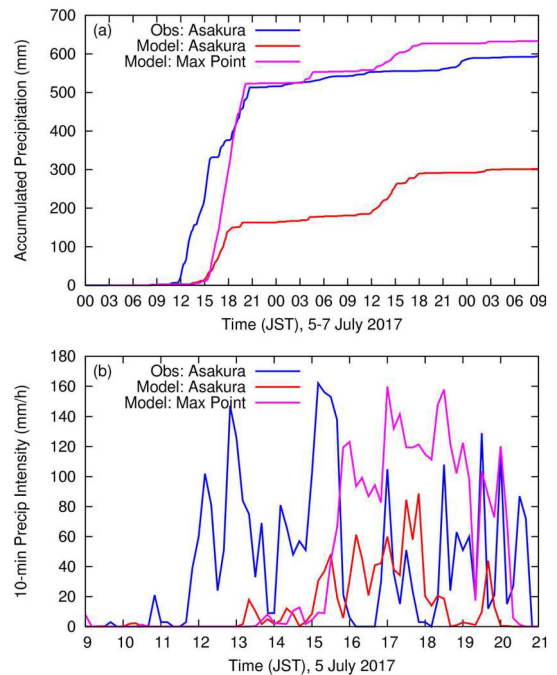


Fig. 2. Time series of (a) accumulated rainfall and (b) rain intensity at the 10-minutes interval. Blue, red, and purple lines denote the observation at Asakura, the simulation at the Asakura gridpoint, and the simulation at the point of the maximum accumulated rainfall.

km east of the Asakura point, was chosen, the simulation better captures the observed temporal change. The rapid increase in the afternoon of 5 July and the gradual increase later on are well reproduced, although the simulated rainfall increases more rapidly during the period of 1200 and 2100 JST 5 July. Figure 2b shows the temporal change of the rain intensity at the 10-minutes interval. After 1200 JST, the observed rain sometimes became stronger than 100 mm h^{-1} , and intense rain continued for 9 hours. The simulation at Asakura also reproduced sustained rain in the afternoon, but the intensity is more reduced than the observation. On the other hand, the simulated rain intensity at the gridpoint of the maximum rainfall indicates extreme intensities comparable to the observation. Although the duration of the simulated intense rain in the afternoon is shorter than the observed, the simulation seems to be successful in reproducing the sustained nature of intense rain in the afternoon.

Generally, heavy rainfalls are induced either by sustained rain

or intense rain or the combination of both (Doswell et al. 1996). In the present case, the longevity and intensity of rainfall both contributed to the extreme rainfall. Thus, it is important to reproduce continuous development of convection and stationarity of convective systems in the simulation. Figures 3a and 3b indicate the continuous development of convection in the limited region of around 130.8°E – 131.0°E with the longitude and time diagram, averaged in the latitude of 33.277°N – 33.390°N . The simulation is able to capture large amounts of rainwater at the lower level and stronger updrafts at the upper level sustained in the 5 July afternoon, which is due to the successful simulation of a stationary convective system as well as its background, synoptic-scale field (see Supplement 2 for the surface fields and the temporal evolution of the rainfall and Supplement 3 and 4 for the radar animations).

The environmental conditions for the stationary convective system are examined in terms of convective available potential energy (CAPE) and precipitable water vapor (PW). In Figs. 3c

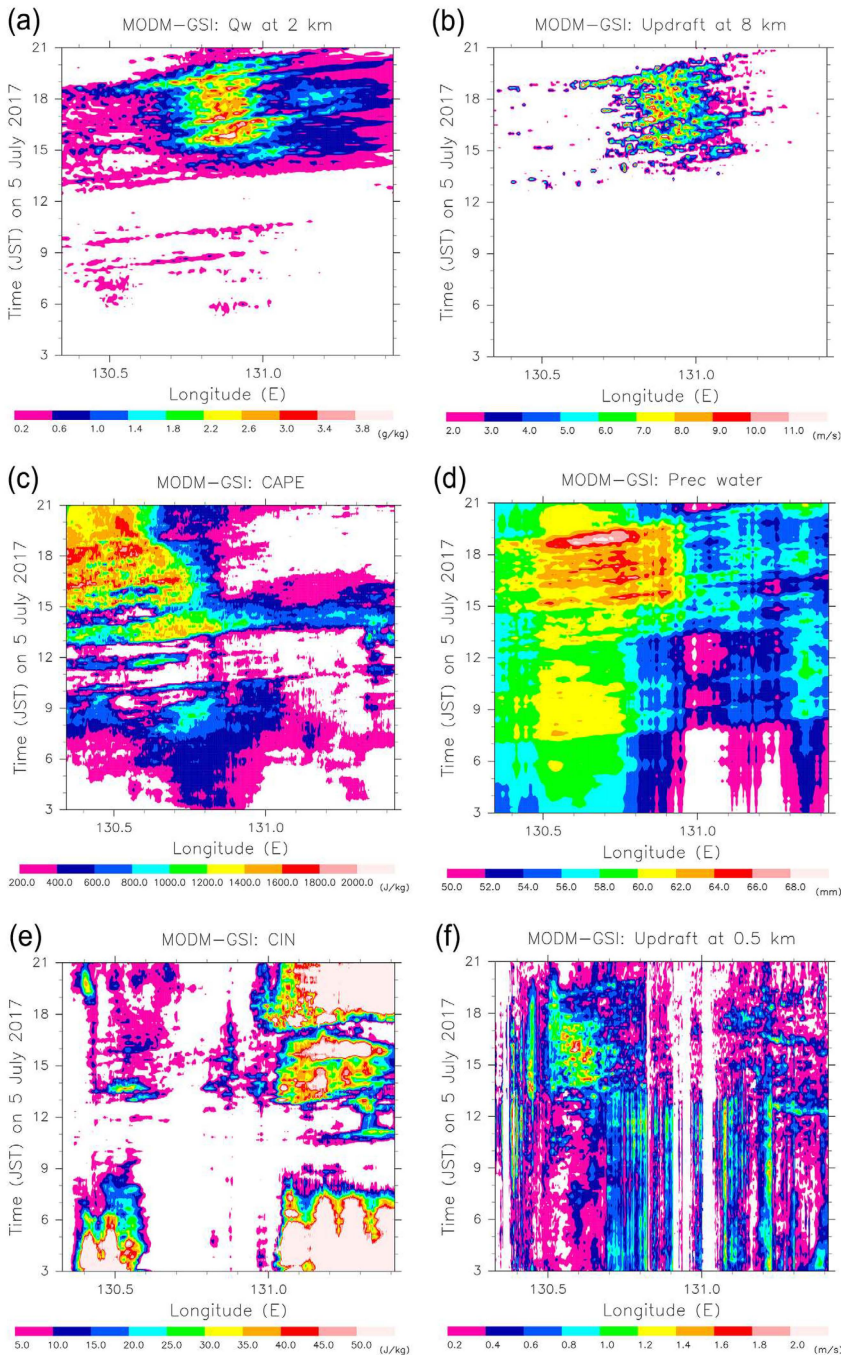


Fig. 3. The longitude and time sections of (a) the total water condensate mixing ratio at the 2-km height, (b) the updraft at the 8-km height, (c) convective available potential energy (CAPE), (d) precipitable water vapor, (e) convective inhibition (CIN), and (f) the updraft at the 0.5-km height obtained from the MODM-GSI experiment. Heights are indicated by the height above the mean sea level.

and 3d, the areas of high CAPE and PW are seen to extend in the upwind side (west) of the convective system, indicating that the atmosphere is very unstable and moist as compared to the climatology at Fukuoka: CAPE = 501 and PW = 51 as the July mean for QSCCs (Unuma and Takemi 2016a).

To diagnose possible triggers for the convection development in terms of convective inhibition (CIN) and low-level updraft, Figs. 3e and 3f shows the longitude and time diagram of CIN and the ascent at the 0.5-km height averaged meridionally between 33.383° – 33.452° (including the small-scale mountains near the west-end of Domain 4). Before the convection development, CIN is almost zero, indicating that convection can easily develop with a minimal forcing. The low-level ascent becomes intensified after 1400 JST and sustained in the region of 130.5° E– 130.7° E which corresponds to the lowland just to the east of the small-scale mountains near the west-end. Therefore, the continuous low-level ascent in the minimal CIN environment is considered to play a triggering role in sustaining the convective system.

4. Sensitivity experiments

The spatial distribution of the accumulated rainfall and the longitude and time section of the low-level water content in MODM-G30 are shown in Figs. 4a and 4b. The spatial pattern and concentrated feature of heavy rainfall around the center of the domain is also seen in Fig. 4a, but the total amount is significantly reduced from that in MODM-GSI. Figure 4b indicates that convection successively develops in the 130.8° E– 131.0° E region; however, discretely developing feature in this region is seen more clearly in MODM-G30 than in MODM-GSI. Besides, the low-level forcing in MODM-G30 (Fig. 4c) is much weaker than that in MODM-GSI (Fig. 3f). Both weaker forcing and discrete development lead to the reduction of the accumulated rainfall.

The comparison between MODM-GSI and MODM-G30 demonstrates that the differences in the continuous convective development and the quantitative rainfall reproduction are attributed to the difference in the terrain representation in the two experiments. One may argue that the impacts of the terrain representation would depend on the settings of the physics parameterizations employed and the initial and boundary conditions. To resolve this concern, we exhibit the results of another set of the numerical experiments, WSM6-GSI and WSM6-G30.

The spatial distribution of the accumulated rainfall and the longitude and time section of the low-level water content for WSM6-GSI and WSM6-G30 are shown in Fig. 5. A large amount of the rainfall around the center of the domain is seen in WSM6-GSI, and the rainfall amount in the same area is significantly reduced in WSM6-G30. Furthermore, the low-level water content becomes smaller and the discrete nature of convection is more

evident in the 130.8° E– 131.0° E region in WSM6-G30 than in WSM6-GSI. Again, the impact of the difference in terrain representation appears in the WSM6 cases as in the MODM cases. Comparing the results of Figs. 1b and 5a or those of Figs. 3a and 5b, the cloud microphysics scheme may affect the quantitative representation of the heavy rainfall, which is due to the difference in convection development in the limited region. There is another point to note that the accumulated rainfall amount near the southern boundary of Domain 4 is similarly represented or is decreased in the GSI or MODM cases compared to the G30 or WSM6 cases.

In this way, the convection development depends on the terrain representation as well as the cloud microphysics scheme. To diagnose this dependence, the precipitation intensity at each output time is examined. Figure 6 compares the frequency distributions of the precipitation intensity obtained in the area of 130.6° E– 131.0° E and 33.3° E– 33.5° E during the simulation time. MODM-GSI reproduced the highest frequencies in stronger rains, especially in the highest range. Use of coarser-resolution terrain data (MODM-G30) or single-moment microphysics scheme (WSM6-GSI) or the both (WSM6-G30) leads to significant reduction in stronger rains. Thus, the decreased frequency of stronger rains and the discretely developing convection within the convective system seem to make the accumulated rainfall in the limited region smaller.

Here we discuss a consequence resulting from the difference in terrain representation between GSI and G30. Figure 7a demonstrates the difference of the model topography between GSI and G30 in a grid-point basis. At or near mountain peaks, the model heights tend to be higher in GSI than in G30. The highest peak in Domain 4 is 1763.6 m for GSI while 1679.6 m for G30. Contrary, the model heights in areas between mountain peaks and lowlands are lower in GSI than in G30, meaning that the terrain feature is more smoothed in G30 than in GSI. This terrain difference will directly influence surface wind fields. Hence, the convergence/divergence of surface winds is examined by focusing the area of 130.5° E– 130.7° E and 33.383° E– 33.452° E, where the low-level ascent was clearly seen. Figure 7b compares the frequency distributions of the convergence/divergence for MODM-GSI and MODM-G30. The frequency of larger magnitudes of convergence (positive values) and divergence (negative) is higher in MODM-GSI than MODM-G30, suggesting that the fine terrain features enhance surface convergence/divergence. We speculate that the enhanced low-level convergence to the west of the area where the stationary convective system developed is due to more sharply represented topography in MODM-GSI than in MODM-G30. A low-flatland surrounded by sharply represented mountains will perform as a guide for the low-level, convergent flow. The enhanced convergence in the area leads to stronger low-level ascents in the GSI case, which serves as a trigger for the convection development for the present heavy rainfall event.

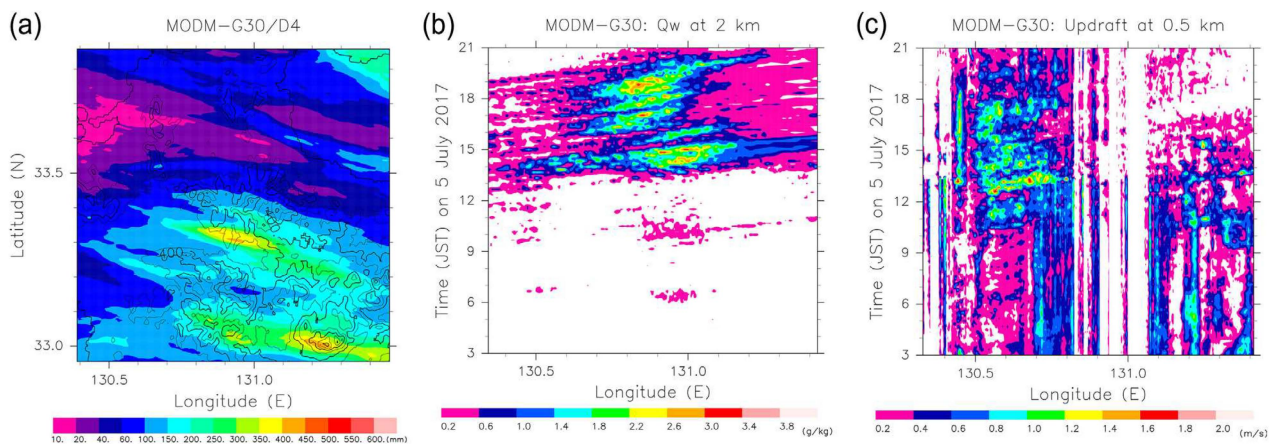


Fig. 4. (a) The accumulated rainfall from 0300 JST 5 July to 0900 JST 7 July 2017 from the MODM-G30 experiment in Domain 4. The terrain height is contoured at 200 m. The longitude and time sections of (b) the total water condensate mixing ratio at the 2-km height and (c) the updraft at the 0.5-km height obtained from MODM-G30.

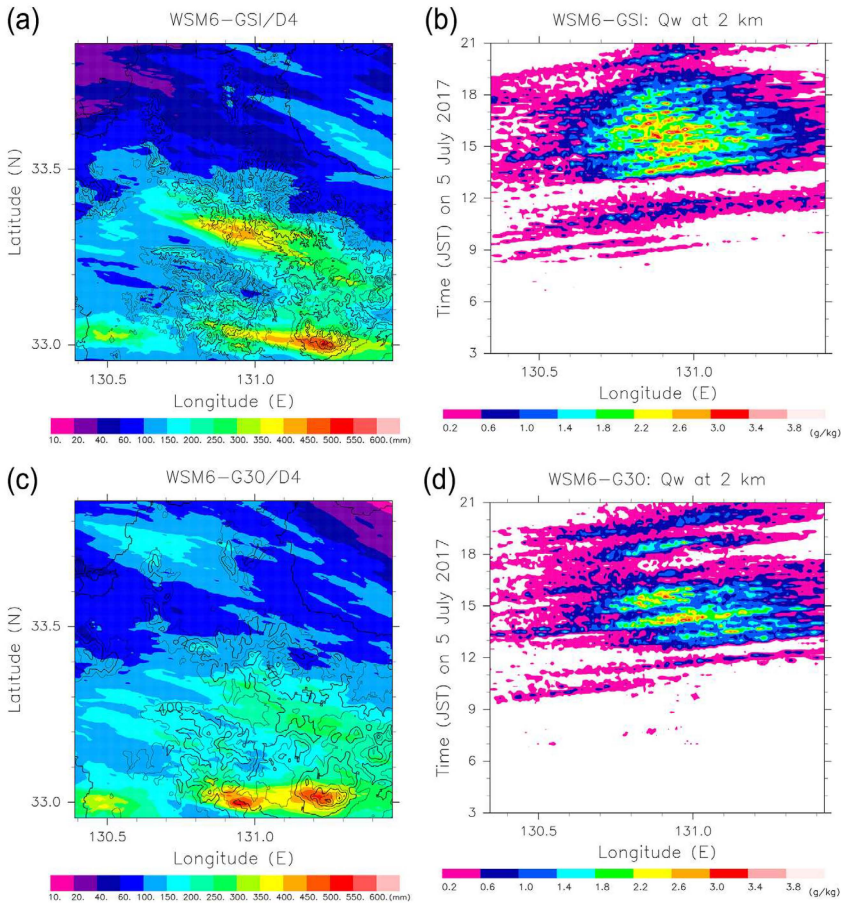


Fig. 5. The accumulated rainfall from 0300 JST 5 July to 0900 JST 7 July 2017 from (a) WSM6-GSI and (c) WSM6-G30 in Domain 4, and the longitude and time sections of the total water condensate mixing ratio at the 2-km height in (b) WSM6-GSI and (d) WSM6-G30. In (a) and (c), the terrain height is contoured at 200 m.

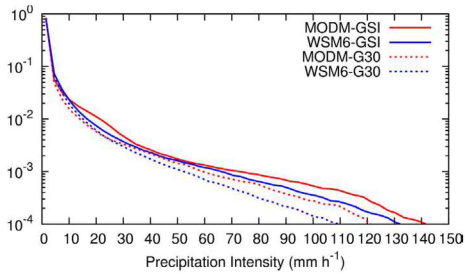


Fig. 6. Frequency distribution of the rain intensity computed at the 10-minutes interval in the area of 130.6°E–131.0°E and 33.3°E–33.5°E for MODM-GSI, MODM-G30, WSM6-GSI, and WSM6-G30 during the simulated time period of Domain 4.

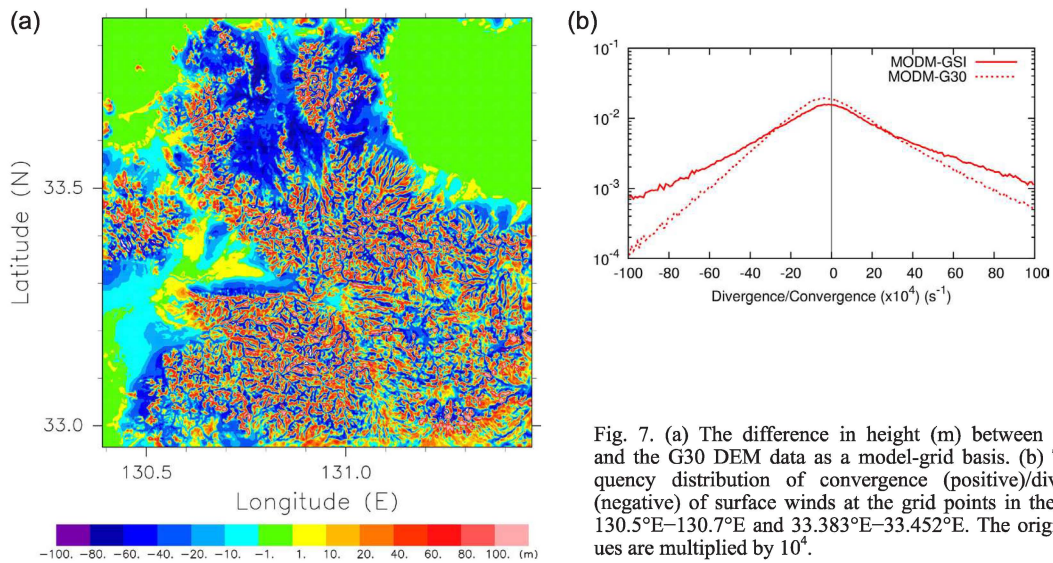


Fig. 7. (a) The difference in height (m) between the GSI and the G30 DEM data as a model-grid basis. (b) The frequency distribution of convergence (positive)/divergence (negative) of surface winds at the grid points in the area of 130.5°E–130.7°E and 33.383°E–33.452°E. The original values are multiplied by 10^4 .

5. Conclusions

We investigate the influences of the terrain representation on the simulations of a stationary convective system and the resulting heavy rainfall for the July 2017 Northern Kyushu case by conducting a series of numerical experiments at the 167-m grid. By employing the 50-m-mesh elevation dataset as well as a double-moment microphysics scheme, the control experiment successfully reproduced the stationary convective system and the associated heavy rainfall. When the GTOPO30 dataset was used, the simulated rainfall was significantly reduced and the convective system indicated a discretely developing feature even with the 167-m grid. The similar impacts of the terrain representation also appeared in the different microphysics scheme case, which strongly suggests that those impacts are robust.

The sensitivity experiments demonstrated that the representation of model terrain is critically important in reproducing stationary convective systems and quantitatively the resulting heavy rainfall in convection-resolving simulations at a $O(100\text{ m})$ grid spacing. However, the use of double-moment scheme or high-resolution DEM data may not always improve the rainfall amount. The impacts of the terrain representation should be more extensively investigated by systematically changing physics parameterizations, analysis fields, initial times, and rainfall cases.

Acknowledgements

The anonymous reviewers' comments were greatly acknowledged to improve the manuscript. This study was supported by JSPS Kakenhi-17K20140/18H01680, Post-K Project, and MEXT TOUGOU Program.

Edited by: C.-C. Wang

Supplement

Supplement 1: Figures showing the computational domains and the surface weather maps.

Supplement 2: Figures comparing the simulated results with the observed features in terms of synoptic-scale patterns at the mean-sea level and radar reflectivity evolution.

Supplement 3: The simulated stationary convective systems from 1200 JST to 2100 JST 5 July 2017 in Domain 4 of MODM-GSI.

Supplement 4: The precipitation radar/raingauge analysis from 1200 JST to 2100 JST July 2017 at 1-hour interval.

References

Doswell, C. A., H. E. Brooks, and R. A. Maddox, 1996: Flash flood forecasting: An ingredients-based methodology. *Wea. Forecasting*, **11**, 560–581.

Hong, S.-Y., and J. O. J. Lim, 2006: The WRF Single-Moment 6-Class Microphysics Scheme (WSM6). *J. Korean Meteor. Soc.*, **42**, 129–151.

Hong, S.-Y., Y. Noh, and J. Dudhia, 2006: A new vertical diffusion package with an explicit treatment of entrainment processes. *Mon. Wea. Rev.*, **134**, 2318–2341.

Houze, R. A., Jr., 2012: Orographic effects on precipitating clouds. *Rev. Geophys.*, **50**, RG1001, doi:10.1029/2011RG000365.

Jiménez, P. A., J. Dudhia, J. F. González-Rouco, J. Navarro, J. P. Montávez, and E. García-Bustamante, 2012: A revised scheme for the WRF surface layer formulation. *Mon. Wea. Rev.*, **140**, 898–918.

Kirshbaum, D. J., G. H. Bryan, R. Rotunno, and D. Durran, 2007: The triggering of orographic rainbands by small-scale topography. *J. Atmos. Sci.*, **64**, 1530–1549.

Morrison, H., G. Thompson, and V. Tatarskii, 2009: Impact of cloud microphysics on the development of training stratiform pre-

cipitation in a simulated squall line: Comparison of one- and two-moment schemes. *Mon. Wea. Rev.*, **137**, 991–1007.

Nagata, K., 2011: Quantitative precipitation estimation and quantitative precipitation forecasting by the Japan Meteorological Agency. *RSMC Tokyo-Typhoon Center Technical Review*, **13**, 37–50. (Available online at: <http://www.jma.go.jp/jma/jma-eng/jma-center/rsmc-hp-pub-eg/techrev/text13-2.pdf>, accessed 24 April 2018)

Oizumi, T., K. Saito, J. Ito, T. Kuroda, and Le Duc, 2018: Ultra-high-resolution numerical weather prediction with a large domain using the K Computer: A case study of the Izu Oshima Heavy Rainfall event on October 15–16, 2013. *J. Meteor. Soc. Japan*, **96**, 25–54.

Oku, Y., T. Takemi, H. Ishikawa, S. Kanada, and M. Nakano, 2010: Representation of extreme weather during a typhoon landfall in regional meteorological simulations: A model intercomparison study for Typhoon Songda (2004). *Hydrol. Res. Lett.*, **4**, 1–5, doi:10.3178/hrl.4.1.

Schumacher, R. S., and R. H. Johnson, 2005: Organization and environmental properties of extreme-rain producing mesoscale convective systems. *Mon. Wea. Rev.*, **133**, 961–976.

Schumacher, R. S., and R. H. Johnson, 2008: Mesoscale processes contributing to extreme rainfall in a midlatitude warm-season flash flood. *Mon. Wea. Rev.*, **136**, 3964–3986.

Skamarock, W. C., J. B. Klemp, J. Dudhia, D. O. Gill, D. M. Barker, M. G. Duda, X.-Y. Huang, W. Wang, and J. G. Powers, 2008: A description of the Advanced Research WRF version 3. *NCAR Tech. Note*, NCAR/TN-47 + STR, 113 pp.

Takemi, T., 2010: The 100-m-mesh numerical simulations of severe local rainstorms by representing complex terrain features. *Ann. Disa. Prev. Res. Inst., Kyoto Univ.*, **53B**, 337–343.

Takemi, T., 2013: High-resolution meteorological simulations of local-scale wind fields over complex terrain: A case study for the eastern area of Fukushima in March 2011. *Theor. Appl. Mech. Japan*, **61**, 3–10, doi:10.11345/nctam.61.3.

Takemi, T., K. Kusunoki, K. Araki, T. Imai, K. Bessho, S. Hoshino, and S. Hayashi, 2010: Representation and localization of gusty winds induced by mesocyclones with a high-resolution meteorological modeling. *Theor. Appl. Mech. Japan*, **58**, 121–130, doi:10.11345/nctam.58.121.

Tsuguti, H., and T. Kato, 2014: Objective extraction of heavy rainfall events and statistical analysis on their characteristic features. *Tenki*, **61**, 455–469. (in Japanese)

Unuma, T., and T. Takemi, 2016a: Characteristics and environmental conditions of quasi-stationary convective clusters during the warm season in Japan. *Quart. J. Roy. Meteor. Soc.*, **142**, 1232–1249.

Unuma, T., and T. Takemi, 2016b: A role of environmental shear on the organization mode of quasi-stationary convective clusters during the warm season in Japan. *Sci. Online Lett. Atmos.*, **12**, 111–115.

Wang, C.-C., G. T.-J. Chen, T.-C. Chen, and K. Tsuboki, 2005: A numerical study on the effects of Taiwan topography on a convective line during the mei-yu season. *Mon. Wea. Rev.*, **133**, 3217–3242.

Wang, C.-C., J. C.-S. Hsu, G. T.-J. Chen, and D.-I. Lee, 2014: A study of two propagating heavy-rainfall episodes near Taiwan during SoWMEX/TiMREX IOP-8 in June 2008. Part II: Sensitivity tests on the roles of synoptic conditions and topographic effects. *Mon. Wea. Rev.*, **142**, 2644–2664.

Yoshizaki, M., T. Kato, Y. Tanaka, H. Takayama, Y. Shoji, and H. Seko, 2000: Analytical and numerical study of the 26 June 1998 orographic rainband observed in western Kyushu, Japan. *J. Meteor. Soc. Japan*, **78**, 835–856.

Yu, C.-K., and B. J.-D. Jou, 2005: Radar observations of the diurnally forced offshore convective lines along the southeastern coast of Taiwan. *Mon. Wea. Rev.*, **133**, 1613–1636.

Yu, C.-K., and C.-Y. Lin, 2008: Statistical location and timing of the convective lines off the mountainous coast of southeastern Taiwan from long-term radar observations. *Mon. Wea. Rev.*, **136**, 5077–5094.

Manuscript received 27 April 2018, accepted 24 September 2018
SOLA: <https://www.jstage.jst.go.jp/browse/sola/>